Commun. Comput. Phys.
doi: 10.4208/cicp.261211.290612a

Vol. **13**, No. 5, pp. 1209-1226
May 2013

Retrieving Topological Information of Implicitly Represented Diffuse Interfaces with Adaptive Finite Element Discretization

Jian Zhang[1,3,*] and Qiang Du[2]

[1] *Supercomputing center, Chinese Academy of Sciences, Beijing, P.R. China.*
[2] *Department of Mathematics, Pennsylvania State University, University Park, PA 16802, USA.*
[3] *State Key Laboratory of Space Weather, Chinese Academy of Sciences, Beijing, P.R. China.*

Received 26 December 2011; Accepted (in revised version) 29 June 2012

Communicated by Jie Shen

Available online 8 October 2012

Abstract. We consider the finite element based computation of topological quantities of implicitly represented surfaces within a diffuse interface framework. Utilizing an adaptive finite element implementation with effective gradient recovery techniques, we discuss how the Euler number can be accurately computed directly from the numerically solved phase field functions or order parameters. Numerical examples and applications to the topological analysis of point clouds are also presented.

AMS subject classifications: 65N30, 57M50, 74A50, 92C05

Key words: Diffuse interface model, phase field method, Euler number, Gauss curvature, adaptive finite element, gradient recovery.

1 Introduction

Efficient and robust numerical simulations of various interfaces have been subject to much research in many applications. Indeed, the geometric and topological properties of interfaces play important roles in many physical and biological processes. For example, in biological science, the geometric shapes of bilayer vesicle membranes have significant roles in cell functions and the signal transduction pathway [11, 30, 32, 34]. Similarly, in materials science, it is well known that material thermomechanical properties depend on the underlying micro-structures characterized by interfaces.

*Corresponding author. *Email addresses:* zhangjian@sccas.cn (J. Zhang), qdu@math.psu.edu (Q. Du)

In recent years, diffuse interface methods have become popular approaches to simulate and model complex interfaces appearing in various applications. A well known example is the diffuse interface description of material interfaces developed by Cahn and Hilliard [6] for phase transition problems. They are also often called phase field models in the materials science community [7]. A distinct feature of the diffuse interface or phase field approach to the modeling of interfaces is that the interfaces are implicitly represented by phase field functions or order parameters so that a single set of equations may be used as the mathematical models on and across the interfaces. There is no explicit tracking of interfaces so that the numerical simulations are also insensitive to the underlying changes of interfacial topology. In the last fifty years, there have been many works related to the various extensions of diffuse interface theory and their applications in diverse fields. Until today, researches remain active on the development of the diffuse interface models for new application problems and their effective numerical implementations, see a number of reviews on the subject [1,7,35,36]. The mathematical and numerical analysis of diffuse interface models have also received much attention, see for instance [3–5,8,16,17,19–21,25,29].

The topological changes of the interfaces can be an important issue in many applications such as the study of fusion and fission of membrane vesicles as well as the study of the microstructure evolution during material phase transitions. In recent years, it has becoming an increasingly interesting topic of research to not only perform the diffuse interface simulations but also to extract useful features of the interfaces from the simulation results, including the crucial topological properties of the interfaces. The latter often involved careful studies of the geometric images obtained from the simulations, see [27] and the references cited therein. Since the diffuse interface approach is insensitive to topological events, it is natural to ask if it is possible to directly extract topological information of the underlying interface from the diffuse interface simulations without resorting to the image reconstruction. In [14], a formula for capturing the Euler number of vesicles within the diffuse interface framework was proposed. Further simplification and analysis were carried out in [15]. The key idea behind such works is based on being able to first formulate and compute the curvatures of the interfaces within the diffuse interface framework, and to then estimate the Euler number through a post-processing of the order parameter (phase field functions) by utilizing the relation between the Euler number and the Gauss curvature given by the Gauss-Bonnet theorem. In the studies reported so far, the numerical simulations were based on Fourier spectral approximations with the spatial derivatives being evaluated via the FFT. Yet, in many engineering and scientific applications of phase field methods, other discretization methods such as finite difference and finite element method have also been widely used. This motivates our current study. We demonstrate here how the Euler number of the implicitly represented interfaces may be effectively computed within an adaptive finite element discretization. We begin with a brief description of some examples of diffuse interface models and its adaptive finite element approximations in Section 2. The diffuse interface Euler formula to be implemented is then presented, following the derivation in [14]. It has a special feature

to allow the integration over domains around the interfaces, thus adaptive discretization methods are particularly attractive as they can provide better resolution to solution in the interfacial region. The detailed algorithmic procedures to compute the Euler number via the post-processing of the finite element approximations are discussed in Section 3. Several important practical issues are addressed in Section 4 through a series of numerical examples, which include the examination on the effect of the interfacial width parameter and the resolution level of the finite element approximations. The examples demonstrate effectiveness of the diffuse interface Euler number in providing robust and accurate topological information on the interface under consideration. Furthermore, we also present some examples of using the Euler number formula to explore the topological structures in data sets to show the potential of our works in other interesting applications.

2 Diffuse Interface, adaptive FEM and the Euler number formula

We now briefly introduce the diffuse interface models. Of particular relevance to the Euler number calculation is that of the elastic bending energy of a vesicle membrane. We then discuss the adaptive finite element solution and meshes of such diffuse interface models and the formula to calculate the Euler number of the vesicle described by the phase field function.

For illustration, let us use a real-valued order parameter ψ (the phase field function) to characterize the two different phases of the material, and take $\psi=\pm 1$ as the ideal values of ψ in the two phases. Then, within the diffuse-interface framework, the total free energy (including the bulk and the interfacial energies) of an inhomogeneous system may be given by [6]:

$$E(\psi)=\int_{\Omega}\left(W(\psi)+\frac{\epsilon}{2}|\nabla\psi|^2\right)dx, \tag{2.1}$$

with W often being a double well potential of the form $W(x)=(x^2-1)^2/4\epsilon$ with wells ± 1 and Ω being the computational domain that encloses the interface which is implicitly determined by the zero level set of the order parameter ψ which is smoothly defined. The small parameter ϵ typically depicts the width of the interfacial layer, that is, regions where the phase field function has large spatial gradient and changes its value from nearly -1 to nearly 1. In the sharp interface limit as $\epsilon\to 0$, the variational problems associated with the particular form of the energy (2.1) leads to that associated with the interface area [20]. In some applications, the dominant interfacial energy may be of forms other than ones related to the interface area. For instance, for a bilayer lipid vesicle membrane, the most relevant energetic contribution to the equilibrium membrane geometry is usually the elastic bending energy of the form [32]:

$$E_{elastic}=k\int_{\Gamma}\frac{H^2}{2}ds, \tag{2.2}$$

where H is the mean curvature of the membrane surface Γ. The parameter k is the bending rigidity, which can depend on the local heterogeneous concentration of the species (such as protein and cholesterol molecules), but it is mostly assumed to be a constant. As proposed in [13], the following phase field elastic energy can be used to approximate $E_{elastic}$,

$$E(\phi)=\int_\Omega \frac{k\epsilon}{2}\left(\triangle\phi-\frac{1}{\epsilon^2}(\phi^2-1)\phi\right)^2 dx. \tag{2.3}$$

The equilibrium vesicle shape, subject to given volume and surface area constraints are determined from the variational problem:

$$\begin{cases} arg\min\limits_{\phi} E(\phi)=\int_\Omega \frac{k\epsilon}{2}\left[\triangle\phi-\frac{1}{\epsilon^2}(\phi^2-1)\phi\right]^2 dx, \\ A(\phi)=\int_\Omega \phi dx=\alpha, \\ B(\phi)=\int_\Omega \left[\frac{\epsilon}{2}|\nabla\phi|^2+\frac{1}{4\epsilon}(\phi^2-1)^2\right]dx=\beta, \\ \phi|_{\partial\Omega}=1, \end{cases} \tag{2.4}$$

where α and β are given constants corresponds to the volume and surface area constraints respectively. We refer to [12] for more discussions on works related to (2.2) and (2.4).

In our previous work [17], we presented an adaptive finite element method for the numerical simulation of vesicle membrane deformation based on the phase field bending elasticity model (2.2). Adaptive methods often lead to efficient discretization to problems with solutions that are singular or have large variations in small scales. In diffuse interface/phase field models, the sharp interface of physical quantities are replaced by regularized phase field functions. However, for small interfacial width constant ϵ, the phase field solutions may display large gradients within the diffusive interfacial region. Thus, adaptivity in the form of mesh refinement and coarsening as well as mesh transformation can greatly improve the efficiency of the numerical approximations of phase field models [4,9,22,25,33]. In [17], a mixed finite element method (FEM) is developed to discretize the phase field bending elasticity model. We used a robust penalty formulation for the volume and surface area constraints. The total energy is

$$J(\phi)=E(\phi)+M_1[A(\phi)-\alpha]^2+M_2[B(\phi)-\beta]^2,$$

where M_1 and M_2 are penalty constants. Let

$$\lambda=2M_1[A(\phi)-\alpha],\ \mu=2M_2[B(\phi)-\beta];\quad \text{and}\quad \mathcal{H}_0=H^1(\Omega)\times H_0^1(\Omega).$$

The mixed formulation is given by

$$\begin{cases} -\sqrt{k\epsilon}\left[<\nabla f,\nabla v>_\Omega+\frac{1}{\epsilon^2}\left(f(3\phi^2-1),v\right)_\Omega\right]+\lambda(1,v)_\Omega-\mu\sqrt{\frac{\epsilon}{k}}(f,v)_\Omega=0, \\ \sqrt{k\epsilon}\left[<\nabla\phi,\nabla w>_\Omega+\frac{1}{\epsilon^2}\left((\phi^2-1)\phi,w\right)_\Omega\right]+(f,w)_\Omega=0, \end{cases} \tag{2.5}$$

where the solution $(f,\phi-1)\in\mathcal{H}_0$ the test function $(v,w)\in\mathcal{H}_0$ and λ,μ converge to the Lagrange multipliers for volume and surface area constraints as M_1 and M_2 go to infinity. Piecewise linear conforming elements are used for both f and ϕ.

$$V_h=W_h=\left\{v\in C^0(\Omega)\cap H^1(\Omega)\ \middle|\ v|_K\in P_1(K),\ \forall K\in J_h\right\},$$

where J_h is a triangulation of $\overline{\Omega}$ consisting of tetrahedra K whose diameters h_K are bounded above by $h=\max_{K\in J_h}h_K$, and $P_1(K)$ denotes the linear function space on element K. A residual type a posteriori error estimator is derived for the development of the adaptive FEM algorithm. It has the particular form:

$$\eta_K=\left\{\left[C_1\sqrt{k\epsilon}\sum_{e\subset\Omega\cap\overline{K}}h_e^{\frac{1}{2}}|e|^{\frac{1}{2}}\left|\left[\frac{\partial f_h}{\partial n}\right]_e\right|+h_K\|\lambda-\frac{\sqrt{k}}{\epsilon^{3/2}}f_h(3\phi_h^2-1)-\mu\sqrt{\frac{\epsilon}{k}}f_h\|_K\right]^2\right.$$
$$\left.+W^2\left[C_2\sqrt{k\epsilon}\sum_{e\subset\Omega\cap\overline{K}}h_e^{\frac{1}{2}}|e|^{\frac{1}{2}}\left|\left[\frac{\partial\phi_h}{\partial n}\right]_e\right|+C_3h_K\|f_h+\frac{\sqrt{k}}{\epsilon^{3/2}}(\phi_h^2-1)\phi_h\|_K\right]^2\right\}^{\frac{1}{2}}. \tag{2.6}$$

When marking the elements to be refined or coarsened, we use an equal distribution strategy. For a detailed discussion on the derivation and implementation of adaptive FEM solver, we refer to [17]. Effectively, the nodes of the adaptive mesh are concentrated near the interface (the membrane surface) so that the number of nodes is significantly reduced, comparing with the number of nodes in the uniform mesh cases, while the resolution of the numerical solution of the adaptive FEM remains at the same level. In the implementation of the adaptive FEM, conforming linear elements on tetrahedral meshes are used for the approximation of the phase function. A typical phase field solution with the adaptive mesh is shown in Fig. 1. The profiles of ϕ on cross sections $z=0$ and $y=0$ are shown in the upper row. The phase function ϕ is nearly 1 outside the surface and -1 inside. The transition from 1 to -1 takes place in an narrow region around the surface (which is the zero level set of ϕ and is plotted in the picture second to the left lower row). The mesh density is plotted in the other 3 pictures in the lower row. The adaptive mesh has high resolution in the transition region where ϕ has large gradients and low resolution where ϕ is flat. A diffuse interface formula for the Euler number of the surface Γ given by the zero level set of a phase function ϕ is provided in [14]. Let us denote the level set of such a phase function by $\Gamma_\mu=\{\phi(x)=\mu\}$ and define $\Omega_c=\{-c<\phi(x)<c\}$ which forms a banded neighborhood around the surface $\Gamma=\Gamma_0$ for $c>0$. For c close to 0, Γ_μ is close to Γ and has the same topology as Γ for all $|\mu|<c$. Now, define

$$M(x)_{ij}=\frac{1}{2\sqrt{2\pi c|\nabla\phi|}}\left(\nabla_i\nabla_j\phi-\frac{\nabla|\nabla\phi|^2\cdot\nabla\phi}{2|\nabla\phi|^4}\nabla_i\phi\nabla_j\phi\right), \tag{2.7}$$

and let

$$G:=\int_{\Omega_c}\Lambda(M(x))dx, \tag{2.8}$$

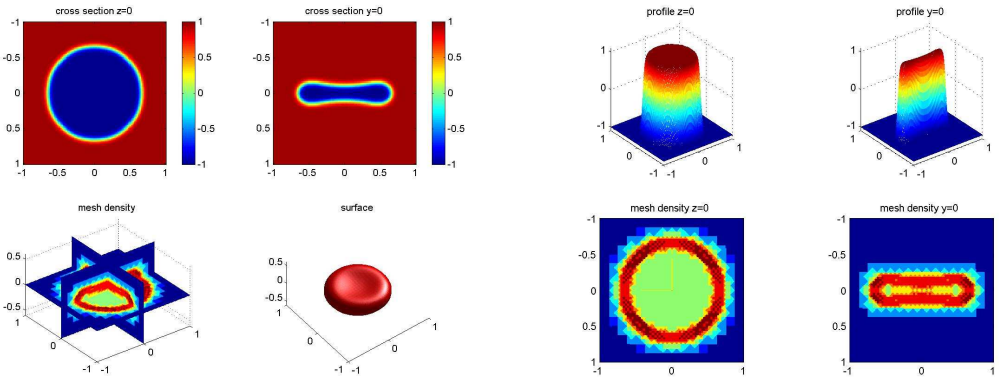

Figure 1: Profile of phase function (upper), mesh density and surface (lower).

where $\Lambda(M)$ is the trace of $(Adj(M))$ which is the adjoint matrix of M. In other words, $\Lambda(M)$ is the sum of the 2×2 principal minors of M. Then for small ϵ, as the phase field function converges to its sharp interface limit, we have

$$\lim_{\epsilon\to 0} G = \frac{\chi}{2} = \frac{1}{4\pi}\int_\Gamma K ds, \tag{2.9}$$

with χ being the Euler number and K being the Gaussian curvature of the surface Γ. The genus (roughly, the number of holes) of the surface Γ can then be approximately determined by

$$genus = 1 - G.$$

We note that more careful interpretation of the formulae (2.8) and (2.9) for self-intersecting or singular surfaces has been given in [14].

3 The AFEM implementation of the diffuse interface Euler number formula

Let Φ^h denote the finite element approximation of the phase function ϕ with h denoting the mesh parameter. For given interfacial width parameter, there have been much studies on the convergence and error estimates of the finite element approximations of various phase field models as $h\to 0$ [9,19,21]. For the phase field bending elasticity model, an error analysis has been provided in [18]. In particular, for the mixed formulation with linear elements (used here), it is shown that with given ϵ, one expects that for some constant c, we have

$$\|\phi - \Phi^h\|_{H^1(\Omega)} \le ch, \tag{3.1}$$

for any h small enough. Moreover, by extending the Aubin-Nitsche trick to nonlinear problems, it is also expected that

$$\|\phi-\Phi^h\|_{L^2(\Omega)}\leq \tilde{c}h^2$$

for a generic constant $\tilde{c}$. Notice that no precise characterization of the dependence of c or $\tilde{c}$ on the parameter ϵ is presently available. Thus, these error analysis are meaningful only in the regime that the interfacial layer has been sufficiently resolved.

Our goal is to calculate the Euler number G using the numerical computed Φ^h. In order to calculate the matrix M in (2.7) associated with Φ^h, we need the first and second order derivatives $\nabla_i\phi$ and $\nabla_i\nabla_j\phi$. Suppose approximations $(\nabla_i\phi)^h$ and $(\nabla_i\nabla_j\phi)^h$ are constructed from Φ^h. In general, suppose V and W are some function spaces related to the discretization. We use

$$(\nabla_i\phi)^h\in V \quad \text{and} \quad (\nabla_i\nabla_j\phi)^h\in W$$

to approximate the first and second derivatives. We can then choose some integral parameter c and calculate the integral in the right hand side of (2.8) for all the elements in Ω_c. In the case that part of an element K is inside Ω_C while another part of it is outside, we calculate the average $\bar{\Phi}^h$ on K and the element is counted if $|\bar{\Phi}^h|<c$.

Since the solution Φ^h is piecewise linear, it is natural to use a piecewise constant function $\nabla_i\Phi^h$ to approximate $\nabla_i\phi$, that is

$$(\nabla_i\phi)^h=\nabla_i\Phi^h\in V^c, \tag{3.2}$$

where V^c denotes the piecewise constant function space related to the space discretization. For the second order derivatives, they usually can be approximated using the L^2 projection on the piecewise linear finite element space V^h. That is,

$$\int_\Omega(\nabla_i\nabla_j\phi)^h\psi dx=-\int_\Omega(\nabla_i\phi)^h\nabla_j\psi dx \quad \text{for all } \psi\in V^h. \tag{3.3}$$

If the piecewise constant approximation (3.2) of $\nabla_i\phi$ is used, the error is of order $\mathcal{O}(h)$ which follows from the error analysis (3.1).

For a nodal basis function ψ, $\nabla_i\psi$ may become of order $\mathcal{O}(1/h)$, then, there could be an $\mathcal{O}(1)$ error in the integrand on the right hand side of (3.3), causing an $\mathcal{O}(1)$ error in the approximation of the second order derivatives. Hence the calculated G may not be convergent when the mesh size h goes to 0. In order to improve the accuracy of $(\nabla_i\nabla_j\phi)^h$, we need a better way to represent $\nabla_i\phi$, that is, to recover the gradients of the finite element solutions with higher accuracy.

Gradient recovery methods with superconvergence property for FEM have been investigated in many existing works, for example [2, 24, 26, 28, 37–40]. In general, better approximations of the gradient can be constructed from the finite element solution Φ^h using various techniques. For an overview of this issue we refer to [2, 28].

In this work, we focus on demonstrating that post-processed (or, recovered) derivatives can be used to calculate G accurately. Thus, we choose to work with the global L^2 projection which allows efficient implementation. For detailed discussions on the rigorous error estimations and analytical background, we refer to [24]. The L^2 projection of the piecewise constant approximation $\nabla_i\Phi^h$ onto the piecewise linear finite element space V^h can be solved from

$$\int_\Omega (\nabla_i\phi)^h\psi dx = \int_\Omega (\nabla_i\Phi^h)\psi dx \qquad \text{for all } \psi\in V^h. \tag{3.4}$$

The solution $(\nabla_i\phi)^h$ is expected to have at lease $o(h)$ accuracy when approximating $\nabla_i\phi$ [24]. Hence we expect to see at least $o(1)$ convergence in G when (3.4), instead of (3.2), is used with (3.3).

In the examples given in next section, we compare the results of using (3.2)-(3.3) with that using (3.3)-(3.4) for the approximations of the derivatives. The results indicate that, as discussed in the above, no convergence in the numerically computed G is observed when (3.2) and (3.3) are used. On the other hand, when (3.3) and (3.4) are used, the error in G becomes significantly smaller and convergence is observed.

4 Numerical results

Here, we present numerical examples to illustrate how various implementation issues in computing the diffuse interface Euler formula can be resolved within the AFEM. We also provide some possible applications to topological data analysis.

4.1 Evaluation of accuracy for simple surfaces

The first series of tests is conducted for a unit sphere. This is a trivial case where we can carefully examine some issues on the accuracy of the numerically computed Euler numbers. For all the examples, the computational domain is taken as $[-1.5,1.5]^3$.

An initial adaptive mesh may be obtained by adaptively updating a coarse uniform mesh several times using a tanh profile of the phase field function $\phi(x) = \tanh((1-|x|)/(\sqrt{2}\epsilon))$ where the interfacial width parameter ϵ is taken to be 0.1. Eq. (2.4) is then solved using adaptive FEM subject to the constraints that the volume is equal to $\frac{4\pi}{3}$ and the area is 4π. We run three simulations with different level of resolution. For the finest resolution level, the initial tanh profile, surface and initial adaptive meshes are shown in Fig. 2 while the profile and surface of the solution and the final adaptive mesh of the simulation is shown in Fig. 3.

We first test the mesh quality by calculating G using exact first and second order derivatives of the tanh profile. The integral limits parameter c takes various values between 0.2 and 0.8. We tested the formula on both initial and final adaptive meshes, the results are shown in Table 1.

Table 1: Computed values of G of a sphere using exact derivatives of a tanh profile.

	c=0.2	c=0.3	c=0.4	c=0.5	c=0.6	c=0.7	c=0.8
	Results for *tanh* profiles on initial meshes						
N=29,949	1.021	1.031	1.026	1.019	1.018	1.010	1.015
N=180,525	1.012	1.006	1.007	1.006	1.006	1.002	1.005
N=552,977	1.004	1.002	1.003	1.002	1.002	1.001	1.000
	Results for *tanh* profiles on final meshes						
N=37,639	1.039	1.011	1.013	1.012	1.004	0.998	0.997
N=223,435	1.031	1.007	1.006	1.006	1.004	1.004	1.004
N=645,915	1.013	1.003	1.002	1.002	1.001	1.001	1.003

Table 2: Computed values of G of a sphere using piecewise constant first order derivatives to construct second order derivatives.

	c=0.2	c=0.3	c=0.4	c=0.5	c=0.6	c=0.7	c=0.8
	Results for *tanh* profiles on initial meshes						
N=29,449	2.409	2.621	2.753	2.890	2.752	2.230	0.316
N=180,525	1.874	2.142	2.481	3.074	3.601	2.690	-0.060
N=552,977	1.670	1.903	2.201	2.632	3.017	2.486	0.902
	Results for numerical solutions on final meshes						
N=37,639	0.176	-0.230	-0.749	-1.469	-2.447	-3.786	-5.509
N=223,435	0.471	-0.063	-0.836	-1.736	-2.783	-4.188	-5.578
N=645,915	0.153	-0.652	-1.812	-3.247	-5.098	-7.357	-9.652

Table 3: Computed values of G of a sphere using piecewise linear first order derivatives to construct second order derivatives.

	c=0.2	c=0.3	c=0.4	c=0.5	c=0.6	c=0.7	c=0.8
	Results for *tanh* profiles on initial meshes						
N=29,449	0.976	0.983	0.970	0.946	0.913	0.865	0.835
N=180,525	1.003	0.998	0.999	0.994	0.967	0.901	0.864
N=552,977	1.001	0.999	0.999	0.999	0.992	0.958	0.878
	Results for numerical solutions on final meshes						
N=37,639	0.957	0.937	0.943	0.947	0.945	0.940	0.930
N=223,435	1.009	0.982	0.982	0.983	0.980	0.975	0.955
N=645,915	1.004	0.994	0.995	0.995	0.993	0.990	0.985

The error of G is less than 3.1% in all cases which indicates the adaptive meshes are good enough to get an accurate G. Here, the integral limit parameter c has little effect on the calculated G. The test results of using such a piecewise constant $(\nabla_i\phi)^h$ via (3.2) in (3.3) are shown in Table 2. We can see the calculated G lacks accuracy and shows no convergence. The results of using piecewise linear $(\nabla_i\phi)^h$ via (3.2) in (3.3) are shown in Table 3. The calculated values of G are reasonably accurate and the convergence of the calculation is evident.

We then conduct numerical tests for a toroidal surface whose Euler number is 0. The

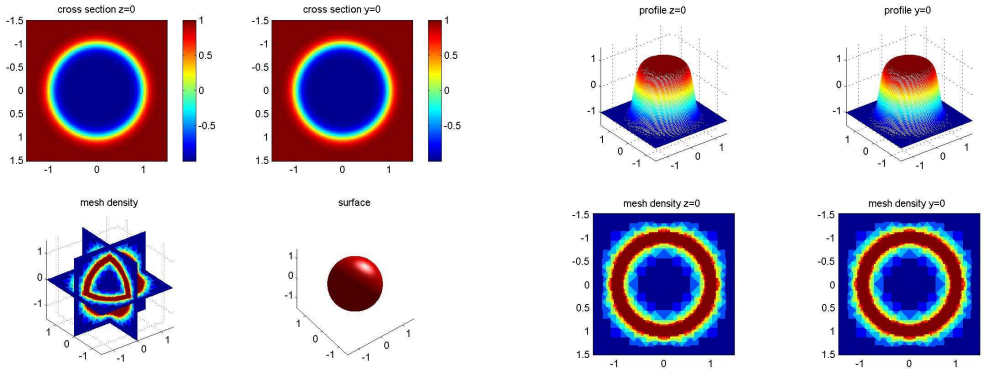

Figure 2: Profile of phase function (upper), mesh density and surface (lower) on initial adaptive mesh. Number of nodes $N=552{,}977$.

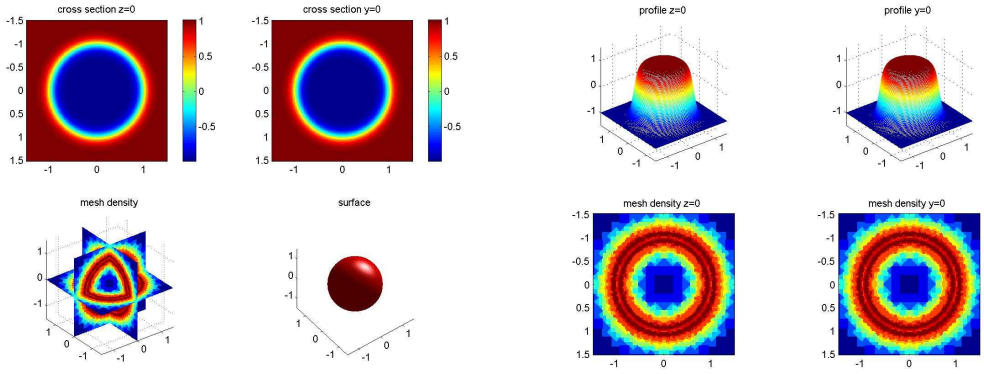

Figure 3: Profile of phase function (upper), mesh density and surface (lower) on final adaptive mesh. Number of nodes $N=645{,}915$.

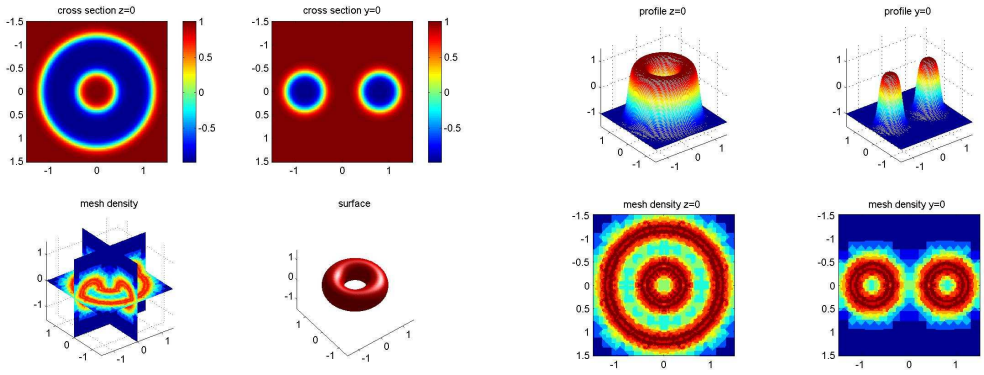

Figure 4: Profile of phase function (upper), mesh density and surface (lower) on final adaptive mesh. Number of nodes $N=554{,}005$.

Table 4: Computed values of G of a torus using piecewise constant first order derivatives to construct second order derivatives.

	c=0.2	c=0.3	c=0.4	c=0.5	c=0.6	c=0.7	c=0.8
	Results for *tanh* profiles on initial meshes						
N=26,907	0.809	0.714	1.089	1.302	1.302	1.237	-0.597
N=152,093	0.331	0.803	1.555	2.171	2.728	2.511	0.012
N=457,697	-1.162	0.715	1.597	3.172	4.220	4.038	1.301
	Results for numerical solutions on final meshes						
N=33,261	-2.493	-3.368	-3.998	-5.011	-6.152	-7.846	-10.60
N=187,529	-2.029	-2.679	-3.889	-5.282	-6.645	-8.804	-11.12
N=554,005	-3.010	-4.068	-5.592	-7.584	-10.04	-13.23	-16.45

Table 5: Computed values of G of a torus using piecewise linear first order derivatives to construct second order derivatives.

	c=0.2	c=0.3	c=0.4	c=0.5	c=0.6	c=0.7	c=0.8
	Results for *tanh* profiles on initial meshes						
N=26,907	-0.075	-0.075	-0.075	-0.124	-0.164	-0.220	-0.293
N=152,093	-0.017	-0.009	-0.011	-0.023	-0.072	-0.157	-0.211
N=457,697	-0.008	-0.001	-0.002	-0.006	-0.020	-0.061	-0.157
	Results for numerical solutions on final meshes						
	c=0.2	c=0.3	c=0.4	c=0.5	c=0.6	c=0.7	c=0.8
N=33,261	-0.023	-0.057	-0.069	-0.063	-0.079	-0.093	-0.123
N=187,529	-0.046	-0.042	-0.039	-0.040	-0.040	-0.054	-0.079
N=554,005	-0.013	-0.013	-0.010	-0.010	-0.011	-0.014	-0.023

tanh profile of the phase function is

$$\phi(x_1,x_2,x_3)=\tanh\left(\frac{r-\sqrt{(\sqrt{x_1^2+x_2^2}-R)^2+x_3^2}}{\sqrt{2}\epsilon}\right),$$

with $R=0.8$, $r=0.4$ and $\epsilon=0.08$. The volume and surface area are set to be $2\pi^2Rr^2$ and $4\pi^2Rr$ respectively. Again we present results corresponding to three different levels of resolution. For simplicity, we only plotted the profile, surface and finial adaptive mesh of the simulation for the finest resolution in Fig. 4. The results of using piecewise constant $(\nabla_i\phi)^h$ in (3.3) are shown in Table 4. Again, the calculated values of G are far off and show no convergence. The results of using piecewise linear $(\nabla_i\phi)^h$ in (3.3) are shown in Table 5 which yield accurate and convergent results.

The numerical tests on the sphere and the torus demonstrate that we can get accurate results using the post-processed $(\nabla_i\phi)^h$ and $(\nabla_i\nabla_j\phi)^h$. Since the nodes of an adaptive mesh are concentrated near the interface, as shown in [17], if the curvatures of the surface do not have significant variation, then it is reasonable to assume that the number of nodes is proportional to the surface area if the level of resolution is kept the same. In our simulations the number of nodes used for the sphere is a little more than those for

Table 6: Computed values of G of a sphere for numerical solutions on final meshes with various ϵ.

ϵ	N	c=0.2	c=0.3	c=0.4	c=0.5	c=0.6	c=0.7	c=0.8
0.1	37,639	0.957	0.937	0.943	0.947	0.945	0.940	0.930
0.071	32,347	0.922	0.915	0.895	0.887	0.884	0.859	0.827
0.071	73,181	0.944	0.922	0.924	0.907	0.898	0.882	0.873
0.071	176,427	0.976	0.942	0.939	0.940	0.940	0.932	0.903
0.05	38,545	0.752	0.732	0.701	0.660	0.605	0.547	0.475
0.05	62,271	0.784	0.773	0.738	0.698	0.641	0.575	0.513
0.05	146,797	0.800	0.789	0.787	0.789	0.793	0.785	0.746
0.05	222,255	0.925	0.911	0.897	0.884	0.871	0.859	0.845

the torus. Notice the surface areas of the sphere and the torus are very close (12.56 and 12.63), but the curvatures of the torus are something larger in magnitude. Moreover the transition width parameter ϵ is 0.1 for the sphere and 0.08 for the torus. Thus, relatively speaking, the meshes used for the sphere are finer than those for the torus so that smaller errors in G can be expected for the sphere than for the torus.

To further illustrate the effect of mesh resolution on the accuracy of G, we run a sequence of simulations for the unit sphere used earlier for various ϵ with a carefully controlled number of nodes N. The results are shown in Table 6 which clearly show that, when ϵ decreases and N is kept at the same level, the accuracy degrades. For the same ϵ, the accuracy improve when N increase.

4.2 Surfaces with more complex topology

We then test the formula on some surfaces with more interesting topology. In these examples, the integral parameter c is taken to be 0.3. The first example is a genus 3 surface with Euler number -2. It corresponds to a minimum bending energy surface subject to suitable volume and surface area constraints. The adaptive finite element solutions of the phase field function are obtained by minimizing the phase field bending energy functional subject to the constraints. The surface is shown in Fig. 5. The calculated G is -2.086 which is obtained from the numerical solution with $N=229{,}399$ and $\epsilon=0.06$.

The solution used for this example is from our previous work with computational domain $[-1,1]^3$. The interfacial width parameter ϵ should be scaled by a factor of 1.5 if one is to compare this example with others.

Next, we test the formula on vesicles with various cavities/inclusions, ranging from small spherical particles to a toroidal shaped cavity to a cavity having a high genus number. The vesicles are shown in Figs. 6, 7 and 8. Some of these cavities are highlighted to be shown individually along with the transparent display of the vesicles. Both the exact Euler number and the calculated diffuse interface Euler number G are stated for comparison purposes, with the latter being obtained from the numerical solutions of the phase field models, respectively with parameters $N=285{,}303$ and $\epsilon=0.06$ for Fig. 6 (left), $N=356{,}041$ and $\epsilon=0.05$ for Fig. 6 (right), $N=432{,}615$ and $\epsilon=0.05$ for Fig. 7, $N=519{,}391$ and $\epsilon=0.05$ for Fig. 8.

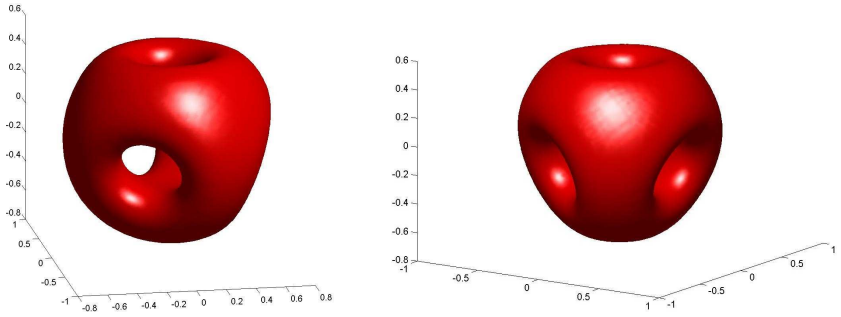

Figure 5: A genus 3 surface viewed from two different angles. Euler number -2, $G=-2.086$.

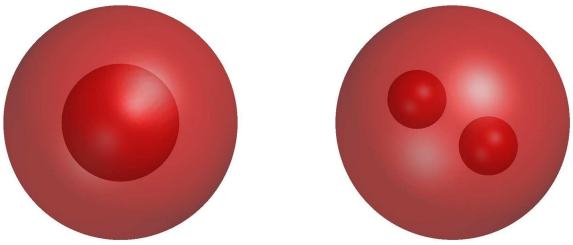

Figure 6: A vesicle containing a single spherical cavity with Euler number 2 and the computed $G=1.960$ (left) and a vesicle having two spherical cavities with Euler number 3 and the computed $G=2.931$ (right).

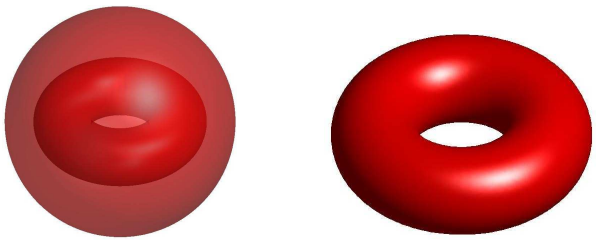

Figure 7: A vesicle containing a toroidal-shaped cavity with the inner surface shown on the right. Euler number 1, $G=0.956$.

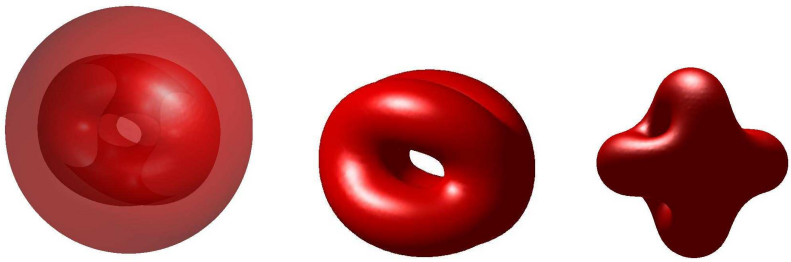

Figure 8: A vesicle containing a high genus cavity with the cavity surface being viewed from two different angles (middle and right). Euler number -1, $G=-1.037$.

4.3 Topological analysis of discrete data sets

The last two examples are related to an interesting application of the phase field model. The objective is to find a surface passing through a set of given points (or point cloud) with minimum energy which consists of both the elastic bending energy and the surface tension as well as a least square fidelity term. The topology of the reconstructed surface can reflect, in some sense, the topological information embedded in the point clouds. For in-depth discussions on the latter, we refer to [10, 23], though the diffuse interface approach differs from those through direct discrete topological constructions.

More specifically, for the phase field model, the total energy consists of three terms, the elastic bending energy $E(\phi)$, the surface tension $\gamma B(\phi)$ and a fidelity (penalty) term:

$$P(\phi)=C\int_{\Omega}\phi^2\sum_i e^{-\frac{|x-x_i|^2}{\delta^2}}dx,$$

where x_i's are the given points and $\delta=\epsilon/5$. The summation in the integrand is an approximation of the characteristic of the set of given points $\{x_i\}$. The penalty term is inactive when x_i falls on the surface because the phase function is close to 0 near the surface, it becomes active otherwise because the phase function is close to either -1 or 1 inside or outside. The total energy $J(\phi)=E(\phi)+\gamma B(\phi)+P(\phi)$ is minimized using adaptive FEM to get a solution ϕ and the zero level-set of ϕ gives the desired surface. The constants γ and C can be adjusted to balance the need of a smooth reconstruction with that of high fidelity to the data set. The weak form (2.5) and the error indicator (2.6) are modified according to the new energy $J(\phi)$.

In the first example, we artificially took 96 points on a torus and randomly made small perturbations to their coordinates to get the set of points x_i's. For the simulations, tee take the interface width parameter $\epsilon=0.05$, the surface tension coefficient $\gamma=10$ and the penalty constant $C=1.0\times10^4$. The resulting surface is plotted in Fig. 9.

Obviously, different values of the interfacial width parameter as well as different numerical resolution levels may lead to reconstructed surfaces with different topology, which, in some sense, may also reflect the topological information in the data set on different scales. We further illustrate this by taking the initial surface being a toroidal surface shown in Fig. 10 and choosing 96 points on the outer ring subject to small random perturbations. When the interface width parameter is big ($\epsilon=0.1$), the inner ring cannot be resolved by the diffuse interface because its radius is too small. Thus, in the reconstructed surface, the hole disappears and the resulting surface has genus 0. The surface defined by the numerical solution and its cross sections are shown in Fig. 11. When the interface width parameter becomes small enough ($\epsilon=0.025$), small features of the data sets can be better identified in the reconstructed surface. In this case, the hole becomes clearly visible so that the computed surface keeps the torus shape and has genus 1. The surface defined by the numerical solution and its cross sections are shown in Fig. 12.

By changing the parameters in the diffuse interface model but maintaining sufficient numerical resolution level, we expect that the topological information extracted from the

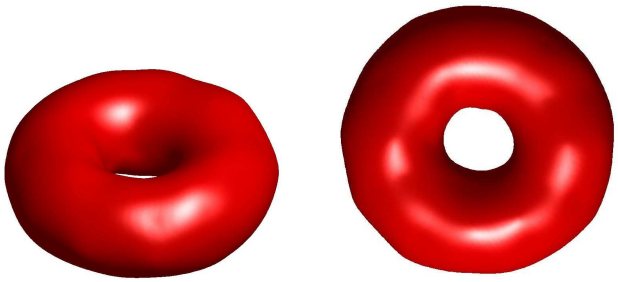

Figure 9: A perturbed torus viewed from two angles. Euler number 0, calculated Euler number $G=-0.098$.

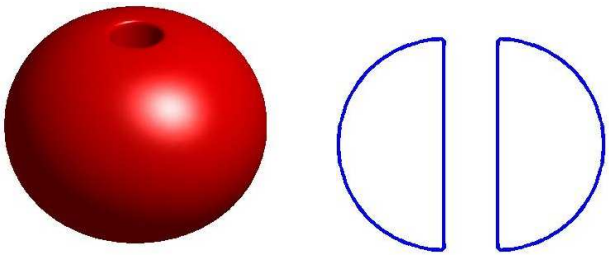

Figure 10: A toroidal surface and its cross section.

diffuse interface can provide descriptions of the topological structure in the data sets on different scales.

5 Conclusion

In this paper we illustrated how the diffuse interface Euler number of a vesicle can be implemented with piecewise linear adaptive finite element discretization. Following the analysis given in [14], it is known that as ϵ gets smaller, the diffuse interface Euler number formula approximates well the exact Euler number of the sharp interface associated with the phase field function. The results given here further demonstrated that, for a given ϵ, when the mesh resolution is good, suitably post-processed first and second order derivatives of the phase field function can be developed to obtain an accurate Euler number. From the presented examples, we also can see that the formula can be used to retrieve topological information for both image and data analysis.

This work is an example of algorithmic development to meet the emerging need for information extraction from numerical simulations. We note that there are many other interesting questions to be studied further, in particular, the Euler number only provides a single topological quantity. It remains to be studied how other topological quantities can also be effectively extracted for implicitly defined surfaces. Developing methodologies that allow the implicit control of the topological features will also be important directions for the future research.

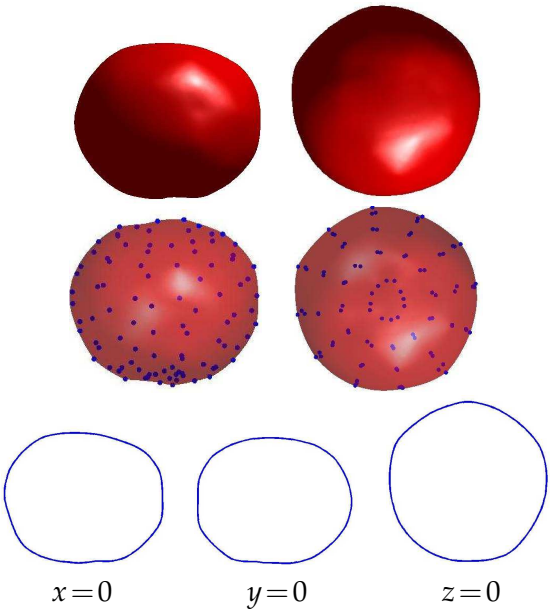

Figure 11: Solution with $\epsilon=0.1$ viewed from two different angles (top row). Solution with $\epsilon=0.1$ viewed from two different angles, where blue dots indicate the location of the 96 perturbed points (second row), and some of its cross sections. Euler number 1, calculated $G=0.883$.

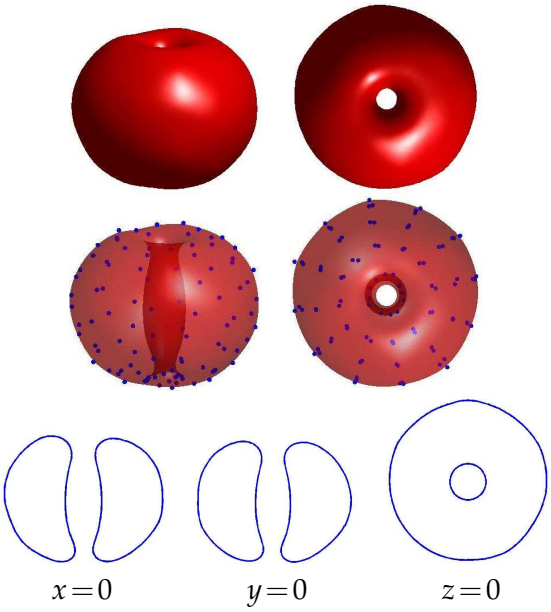

Figure 12: Solution with $\epsilon=0.025$ viewed from two different angles (top row) Solution with $\epsilon=0.025$ viewed from two different angles, where blue dots indicate the location of the 96 perturbed points (second row), and some of its cross sections. Euler number is 0 and the calculated $G=-0.122$.

Acknowledgments

This research is supported in part by US NSF-DMS 1016073, NSFC 11271350 and 91130019, Special Research Funds for State Key Laboratories Y22612A33S, China 863 project 2010AA012301 and 2012AA01A304, China 973 project 2011CB309702.

References

[1] D. Anderson, G. McFadden and A. Wheeler, Diffuse-interface methods in fluid mechanics, Annual Review of Fluid Mechanics, 30: 139-165 (1998).
[2] I.Babuška and T. Strouboulis, The Finite Element Method and its Reliability, Oxford University Press, London (2001).
[3] J. W. Barrett, J. F. Blowey, and H. Garcke, Finite element approximation of the Cahn-Hilliard equation with degenerate mobility, SIAM J. Numer. Anal. 37 (1999), pp. 286-318.
[4] R. J. Braun and B. T. Murray, Adaptive phase-field computations of dendritic crystal growth, Journal of Crystal Growth, 174 (1997), pp. 41-53.
[5] G. Caginalp and X. F. Chen, Phase field equations in the singular limit of sharp interface problems, In On the evolution of phase boundaries (Minneapolis, MN, 1990-91), pp. 1-27. Springer, New York, 1992.
[6] J. W. Cahn and J. E. Hilliard, Free energy of a nonuniform system. I. Interfacial free energy, J. Chem. Phys. 28 (1958), 258-267.
[7] L.Q. Chen, Phase-field models for microstructure evolution, Annual Review of Materials Science, 32 (2002), pp. 113–140.
[8] L.Q. Chen and J. Shen, Applications of semi-implicit Fourier-spectral method to phase field equations, Computer Physics Communications, 108 (1998), pp. 147-158.
[9] Z. Chen, R. Nochetto and A. Schmidt, Error control and adaptivity for a phase relaxation model, M2AN, 34 (2000), 775-797.
[10] A. Collins, A. Zomorodian, G. Carlsson and L. Gulbas, A barcode shape descriptor for curve point cloud data, Computers and Graphics, 28 (2004), 881-894.
[11] H. Döbereiner, E. Evans, M. Kraus, U. Seifert, and M. Wortis, Mapping vesicle shapes into the phase diagram: a comparison of experiment and theory, Phys. Rev. E, 55, pp. 4458–4474, 1997.
[12] Q. Du, Phase field calculus, curvature-dependent energies, and vesicle membranes, Philosophical Magazine, 91 (2011), pp. 165-181.
[13] Q. Du, C. Liu and X. Wang, A phase field approach in the numerical study of the elastic bending energy for vesicle membranes, Journal of Computational Physics, 198, pp. 450–468, 2004.
[14] Q. Du, C. Liu and X. Wang, Retrieving topological information for phase field model, SIAM J. Appl. Math., 65, pp. 1913-1932, 2005.
[15] Q. Du, C. Liu, R. Ryham and X. Wang, Diffuse Interface Energies Capturing the Euler Number: Relaxation and Renomalization, Comm. Math. Sci., 5, pp. 233-242, 2007.
[16] Q. Du and R. Nicolaides, Numerical analysis of a continuum model of phase transition, SIAM J. Num. Anal. 28 (1991), pp. 1310-1322.
[17] Q. Du and J. Zhang, Adaptive Finite Element Method for a Phase Field Bending Elasticity Model of Vesicle Membrane Deformations, SIAM J. Sci. Comp., 30, pp. 1634-1657, 2008.

[18] Q. Du and L. Zhu, Analysis of a Mixed Finite Element Method for a Phase Field Elastic Bending Energy Model of Vesicle Membrane Deformation, J. Computational Mathematics, 24, pp. 265-280, 2006.
[19] C. Elliott and D. French, Numerical studies of the Cahn-Hilliard equation for phase separation, IMA Journal of Applied Mathematics, 38, 97-128, 1987.
[20] L.C. Evans, H. M. Soner, and P. E. Souganidis, Phase transitions and generalized motion by mean curvature Comm. Pure Appl. Math., 45, pp. 1097-1123, 1992.
[21] X Feng and A Prohl, Error analysis of a mixed finite element method for the Cahn-Hilliard equation, Numerische Mathematik, 99, pp. 47-84, 2004.
[22] W.M. Feng, P. Yu, S.Y. Hu, Z.K. Liu, Q. Du and L.Q. Chen, Spectral Implementation of An Adaptive Moving Mesh Method for Phase-field Equations, 220 (2006), 498-510.
[23] R. Ghrist, Barcodes: The persistent topology of data, Bull. Amer. Math. Soc., 45 (2008), 61-75.
[24] B. Heimsund, X.-C. Tai and J. Wang, Superconvergence for the gradient of finite element approximations by L2 projections, SIAM J. Numer. Anal., 40, pp. 1263-1280, 2003.
[25] W. Hu, R. Li and T. Tang, A multi-mesh adaptive finite element approximation to phase field models, Communications in Computational Physics, 5, pp. 1012-1029, 2009.
[26] G. Kunert and S. Nicaise, Zienkiewicz - Zhu error estimators on anisotropic tetrahedral and triangular finite element meshes, ESAIM: Mathematical Modelling and Numerical Analysis, 37 (2003), 1013-1043.
[27] Y. Kwon, K. Thornton and P. Voorhees, The topology and morphology of bicontinuous interfaces during coarsening, Euro. Phys. Lett., 86, 46005, 2009.
[28] A. M. Lakhany, I. Marek, and J. R. Whiteman, Superconvergence results on mildly structured triangulations, Comput. Methods Appl. Mech. Engrg., 189 (2000), pp. 1-75.
[29] J. Lowengrub and L. Truskinovsky, Quasi-incompressible Cahn-Hilliard fluids and topological transitions, R. Soc. Lond. Proc. Ser. A Math. Phys. Eng. Sci., 454 (1998), pp. 2617-2654.
[30] R. Lipowsky, The conformation of membranes, Nature, 349, 475-481, 1991.
[31] O. Mouritsen, Life - As a Matter of Fat: The Emerging Science of Lipidomics, Springer, Berlin, 2005.
[32] Z. Ou-Yang, J. Liu, and Y. Xie, Geometric Methods in the Elastic Theory of Membranes in Liquid Crystal Phases, World Scientific, Singapore, 1999.
[33] N. Provatas, N. Goldenfeld and J. Dantzig, Efficient Computation of Dendritic Microstructures Using Adaptive Mesh Refinement, Phys. Rev. Lett., 80 (1998), 3308-3311.
[34] U. Seifert, K. Berndl and R. Lipowsky, Configurations of fluid membranes and Vesicles, Phys. Rev. A, 44, pp. 1182-1202, 1991.
[35] I. Steinbach, Phase-field models in materials science, Modelling Simul. Mater. Sci. Eng., 17, pp. 073001, 2009.
[36] J. Taylor, Some Mathematical Challenges in Materials Science, Bull. of AMS, 40, 69-87, 2003.
[37] R. Verfürth, A Posteriori Error Estimation and Adaptive Mesh Refinement Techniques, Teubner Skripten zur Numerik, B.G. Teubner, Stuttgart (1995).
[38] Z. Zhang and A. Naga, A new finite element gradient recovery method: superconvergence property, SIAM J. Sci. Comput., 26, pp. 1192-1213, 2005.
[39] O.C. Zienkiewicz and J.Z. Zhu, The superconvergence patch recovery and a posteriori error estimates. part 1: the recovery technique, Int. J. Numer. Methods Engrg., 33, pp. 1331-1364, 1992.
[40] O. C. Zienkiewicz and J. Z. Zhu, The superconvergent patch recovery and a posteriori error estimates. Part 2: Error estimates and adaptivity, Int. J. Numer. Methods Engrg., 33 (1992), pp. 1365-1382.